

Efficient methane oxidation to formaldehyde via photon–phonon cascade catalysis

Received: 20 October 2023

Accepted: 28 June 2024

Published online: 18 July 2024

Check for updates

Youxun Xu¹, Chao Wang¹, Xiyi Li¹, Lunqiao Xiong², Tianyu Zhang³✉, Liquan Zhang⁴, Qinghua Zhang⁵, Lin Gu⁶, Yang Lan¹✉ & Junwang Tang^{1,2}✉

The oxidation of methane to value-added chemicals provides an opportunity to use this abundant feedstock for sustainable petrochemistry. Unfortunately, such technologies remain insufficiently competitive due to a poor selectivity and a low yield rate for target products. Here we show a photon–phonon-driven cascade reaction that allows for methane conversion to formaldehyde with an unprecedented productivity of 401.5 $\mu\text{mol h}^{-1}$ (or 40,150 $\mu\text{mol g}^{-1} \text{h}^{-1}$) and a high selectivity of 90.4% at 150 °C. Specifically, with a ZnO catalyst decorated with single Ru atoms, methane first reacts with water to selectively produce methyl hydroperoxide via photocatalysis, followed by a thermodecomposition step yielding formaldehyde. Single Ru atoms, serving as electron acceptors, improve charge separation and promote oxygen reduction in photocatalysis. This reaction route with minimized energy consumption and high efficiency suggests a promising pathway for the sustainable transformation of light alkanes.

Methane, the primary constituent of shale gas/methane hydrate, is abundant on Earth. Its transformation into high-value liquid chemicals and fuels through a low-carbon process represents a promising pathway for the economic maximization of fossil feedstocks and for substantial reductions in greenhouse gas emissions¹. As a high-volume derivative of methane, formaldehyde (HCHO) is a crucial precursor in the production of industrial resins and plastics. It is also instrumental in applications within the textile and pharmaceutical industries. The current industrial process is an indirect one, necessitating initial steam reforming of methane at high temperatures and under high pressure to produce synthesis gas. The synthesis gas proceeds to produce methanol, which is further oxidized to HCHO over silver-based or iron-molybdate-based catalysts at temperatures around 350 °C (Supplementary Fig. 1)². More than 30% of methanol consumption results from HCHO production via this process^{3,4}. Nevertheless, this multi-step process is inherently energy-consuming and is economically feasible only on a large scale, which is impractical for localized and/or on-site applications, such as

those necessary for preventing flaring of off-gas in remote oil extraction facilities.

Direct oxidation of methane into HCHO, bypassing the synthesis gas and methanol oxidation stages, could make the process eco-friendlier and more efficient. Nonetheless, due to the chemical inertness and high binding energy of the C–H bond (439 kJ mol⁻¹), the thermal activation of methane over molybdenum-oxide-based, vanadium-oxide-based and other metal-oxide-based catalysts as well as phosphate-based catalysts requires temperatures exceeding 500 °C (refs. 5–8). This, unfortunately, leads to the overoxidation of HCHO to CO and CO₂, which results in a selectivity of HCHO down to less than 65% (refs. 9–11). Photocatalysis, using photons as an energy source, can activate and convert methane to oxygenates or hydrocarbons under mild conditions. Recently, methane has been upgraded to HCHO via photocatalysis by various metal oxide semiconductors, such as TiO₂, ZnO, WO₃, In₂O₃ and BiVO₄ (refs. 12–16). A high selectivity of ~90% was achieved over bi-phase TiO₂, Au-modified In₂O₃ and single-atom

¹Department of Chemical Engineering, University College London, London, UK. ²Industrial Catalysis Center, Department of Chemical Engineering, Tsinghua University, Beijing, China. ³College of Environmental Science and Engineering, Beijing Forestry University, Beijing, China. ⁴Department of Chemistry, University College London, London, UK. ⁵Beijing National Laboratory for Condensed Matter Physics, Institute of Physics, Chinese Academy of Sciences, Beijing, China. ⁶Beijing National Center for Electron Microscopy and Laboratory of Advanced Materials, Department of Materials Science and Engineering, Tsinghua University, Beijing, China. ✉e-mail: tzhang@bjfu.edu.cn; yang.lan@ucl.ac.uk; jwtang@tsinghua.edu.cn

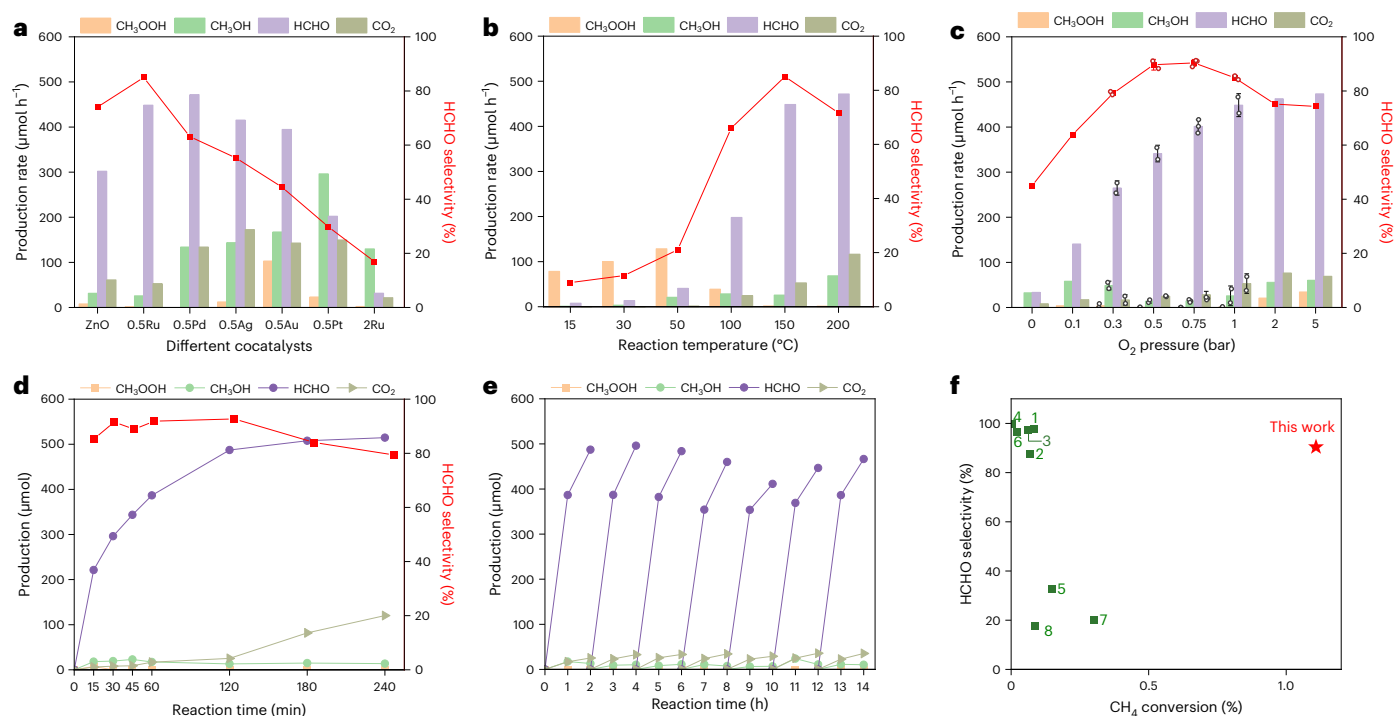


Fig. 1 HCHO production from methane oxidation by photon-phonon-driven cascade catalysis. **a**, The production rate of methane oxidation products over different cocatalyst-loaded ZnO species and their selectivity to HCHO operated at 150 °C. **b**, Influence of reaction temperatures on the production rate and selectivity of HCHO over 0.5Ru-ZnO. The following reaction conditions were used: 10 mg photocatalyst, 180 ml water, 20 bar CH₄, 1 bar O₂, 365 nm LED (75 mW cm⁻², illumination area of 12.56 cm²), 1 h reaction. **c**, The effect of O₂ partial pressure on the reaction over 0.5Ru-ZnO with a fixed CH₄ pressure of 20 bar. The error bars for the 0.75 bar O₂ condition were obtained from three

independent reactions; those for the other conditions were obtained from two independent reactions. The data are presented as mean values ± standard error of the mean. **d**, The product yield over 0.5Ru-ZnO versus the reaction time with 0.75 bar O₂ and 20 bar CH₄. **e**, The stability test of the 0.5Ru-ZnO catalyst for 14 h with each cycle lasting 2 h. **f**, Summary of CH₄ conversion and HCHO selectivity over the reported benchmark photocatalysts. The numbered data points are as follows: (1) Au₂/In₂O₃ (ref. 16), (2) q-BiVO₄ (ref. 12), (3) TiO₂ (90%A + 10%R) (ref. 13), (4) WO₃ (ref. 14), (5) Au/ZnO (ref. 15), (6) Cu-def-WO₃ (ref. 17), (7) AuCu-ZnO (ref. 30) and (8) Pd-def-In₂O₃ (ref. 25).

Cu-modified defective WO₃ (refs. 13,16,17), due to the unique reaction pathway induced by photogenerated electrons and holes. However, the production rate of HCHO remained relatively low (~20 μmol h⁻¹), and the prolonged reaction time led to the overoxidation of HCHO to CO₂ due to the sluggish desorption of HCHO from the catalyst surface at room temperature¹⁶. To enhance the production rate of methane to HCHO through photocatalysis, thus promoting its practical application, the introduction of phonon energy is reasonable due to the enhanced reaction kinetics. More importantly, the first C–H bond dissociation is the rate-determining step in methane conversion, and thermal catalysis cannot overcome this energy barrier under mild conditions, while photocatalysis can readily do it thanks to the quantum effect of photons¹⁸. However, photocatalysis can easily induce overoxidation of the valuable products to CO₂ due to the strong oxidation potential of the photoholes in a semiconductor if the reaction time is extended, whereas phonon energy can effectively tune the selectivity under mild conditions due to the fast desorption of the products at an elevated temperature. The ideal process is therefore a cascade process, in which photocatalysis initiates the first C–H dissociation, leading to one intermediate. Following that, phonon energy continues to convert the intermediate to the desired product against CO₂, resulting in high selectivity of the final product. Combining the benefits of consecutive photocatalysis and phonon-driven transformation could allow us to selectively and efficiently produce HCHO from methane by designing integrated active catalysts to utilize both photons and phonons.

Here, to couple photocatalysis with a phonon-driven decomposition step (photon-phonon-driven cascade catalysis), we designed a photocatalyst substrate (ZnO) modified by catalytically active sites (Ru) for the highly efficient and selective production of HCHO from

methane in one step. With the synergistic effect of photons and phonons, a remarkable HCHO production rate of 401.5 μmol h⁻¹ with a high selectivity of 90.4% is acquired over Ru single atoms (Ru_{SA})-ZnO operated at 150 °C. After CH₃OOH is produced via a photocatalytic process, it is selectively converted into HCHO by a phonon-driven decomposition step, leading to a nearly 30-fold increase in the yield of HCHO and a nearly eightfold improvement in selectivity. Thus, by combining the high selectivity of photocatalysis with the high reactivity of thermodecomposition, this work realizes highly efficient and selective oxidation of methane to HCHO under mild conditions.

Results

Methane oxidation to HCHO over Ru-ZnO

Figure 1a shows the production rate and selectivity of HCHO from methane oxidation over different metal-loaded ZnO species. The setup of the reaction system is shown in Supplementary Fig. 2. HCHO and other liquid products were quantified using the calibration curves in Supplementary Fig. 3. For pure ZnO, HCHO is the primary product (302.1 μmol h⁻¹), whereas CH₃OH (31.5 μmol h⁻¹) and CO₂ (61.2 μmol h⁻¹) rank as minor ones. Upon loading of Pd, Ag, Au and Pt, there was a gradual increase in the production rate of methanol, while the yield of CO₂ also rose, leading to a lower HCHO selectivity. Ru generated more HCHO and reduced the production of CH₃OH and CO₂, exhibiting an impressive selectivity of 85.0% towards HCHO. Only minute quantities of HCOOH and CO were detected (Supplementary Figs. 3c and 4). Subsequently, the Ru loading amount was optimized; the optimized amount is 0.5 wt% (Supplementary Fig. 5a). High Ru loading amounts (>2 wt%) result in high selectivity of CH₃OH. However, the main product is CH₃OOH over 0.5Ru-ZnO at 30 °C (Supplementary Fig. 6), while the

principal products remain CH₃OH and HCHO over 2Ru-ZnO (Supplementary Fig. 5b). ZnO loaded with Au, Pd, Pt and Ag shows a similar product trend to 2Ru-ZnO (Supplementary Fig. 7). The variation in the product selectivity between low Ru and high Ru loading amounts indicates different functions of Ru species across the Ru loading range, which we discuss later.

The impact of temperature was examined over the selected 0.5Ru-ZnO catalyst (Fig. 1b). When the reaction temperature increased from 15 °C to 150 °C, the production rate of all products was enhanced roughly sixfold. Notably, the product distribution at temperatures below 100 °C differed from that at temperatures exceeding 100 °C (Supplementary Fig. 8). At 15 °C, the primary product was CH₃OOH with a selectivity of 89%, while HCHO amounted to only 9%. When the temperature rose to 30 °C and 50 °C, the production rates of HCHO rose to 13.7 μmol h⁻¹ and 40.8 μmol h⁻¹, with selectivities of 11.5% and 21.0%, respectively. The production rate of HCHO reached 198.0 μmol h⁻¹ with a selectivity of 66.0% at 100 °C, while the production rate of CH₃OOH dwindled to 39.0 μmol h⁻¹ with a selectivity of 14.4%. When the temperature increased to 150 °C, the production rate of HCHO further escalated to 448.5 μmol h⁻¹ with a high selectivity of 85.0%. At 200 °C, the production rate of HCHO increased, but a dramatic rise in CO₂ production (~18%) resulted in a low HCHO selectivity of 71.7%. The optimal reaction temperature is thus 150 °C. This indicates that CH₃OOH is transformed to HCHO at higher temperatures, suggesting that CH₃OOH is prone to decomposing under higher-temperature conditions^{19–21}.

Following this, the O₂-to-CH₄ ratio was tweaked to increase HCHO selectivity (Fig. 1c). At lower O₂ pressures (<0.75 bar), only a limited CO₂ production rate was detected. The highest HCHO selectivity of 90.4% was achieved at an O₂ pressure of 0.75 bar, with a production rate of 401.5 μmol h⁻¹. Control experiments in the absence of light, methane or catalysts were conducted (Supplementary Fig. 9). Only trace quantities of HCHO and CO₂ were detected under these conditions, substantiating the idea that HCHO originates from CH₄ and that the process is predominantly induced by photocatalysis rather than thermocatalysis. We also investigated methane conversion and found that 0.5Ru-ZnO had a high methane conversion of 1.1% at 20 bar of methane after 1 h of reaction (Supplementary Fig. 10).

Figure 1d shows the HCHO production over time. In the first 60 min, the HCHO production rate is very high (~400 μmol h⁻¹) because a high concentration of methane and a low concentration of products exist. The average HCHO production rate from 60 to 120 min drops to ~100 μmol h⁻¹ due to accumulated HCHO on the surface of the catalysts. Further extending the reaction time (>120 min), the production of formaldehyde nearly stops increasing, while the production of CO₂ increases rapidly. This is because of the oxidation of HCHO when its concentration is rather high. Similar reaction trends were observed in the thermocatalytic oxidation of methane to methanol²². The results of HCHO oxidation in the presence and absence of methane confirm that the HCHO concentration in the reaction system notably influences the reaction kinetics (Supplementary Fig. 11). The stability of 0.5Ru-ZnO was also assessed (Fig. 1e, Supplementary Figs. 12 and 13, and Supplementary Tables 1 and 2). The 0.5Ru-ZnO catalyst displays constant activity over seven cycles, indicating its excellent stability. The used 0.5Ru-ZnO photocatalyst was subsequently characterized using X-ray diffraction (XRD) and X-ray photoelectron spectroscopy (XPS). Both the phase structure of ZnO and the chemical valency of Ru remained consistent in 0.5Ru-ZnO after the long-term reaction (Supplementary Figs. 14 and 15). The performance of 0.5Ru-ZnO was compared with efficient catalysts previously reported for HCHO production from methane via either photocatalysis or thermocatalysis. Overall, 0.5Ru-ZnO showed a high methane conversion of 1.1% after 1 h of reaction, with a remarkable selectivity exceeding 90%. This represents a methane conversion that is an order of magnitude higher than those of previously documented photocatalysts with a high HCHO selectivity (Fig. 1f and Supplementary Table 3). Such high methane

conversion is also comparable to that achieved by thermal catalysts operated at temperatures beyond 500 °C (Supplementary Fig. 16 and Supplementary Table 3), while the selectivity of HCHO (>90%) is somehow higher than that achieved by thermocatalysis (<65%).

Characterization of photocatalysts

ZnO presents an absorption edge at 400 nm (Fig. 2a). Pronounced absorption throughout the visible spectrum is noticeable over 0.5Ru-ZnO and 2Ru-ZnO, probably due to the scattering effect of Ru. The XRD pattern of ZnO reveals that all peaks correspond to the hexagonal wurtzite phase (JCPDS no. 99-0111) of ZnO (Fig. 2b). No new peaks for Ru were discernible over 0.5Ru-ZnO and 2Ru-ZnO, due to the high dispersion or small particle sizes of Ru. XPS analysis was performed to further investigate the chemical states of Ru species. The C 1s spectrum of ZnO can be split into four peaks, corresponding to C=O, C–O, C–C and Zn–C, which is due to the residual C doping after the calcination of zinc oxalate at low temperatures²³. An extra peak at 281.4 eV was identified as Ru⁴⁺ over 0.5Ru-ZnO, while two peaks of Ru⁴⁺ and Ru⁰ (280.5 eV) were observed in 2Ru-ZnO (Fig. 2c)²⁴. These results suggest that the Ru species are in the Ru⁴⁺ state over 0.5Ru-ZnO and in a mixed state of Ru⁴⁺ and Ru⁰ over 2Ru-ZnO.

Transmission electron microscopy (TEM) shows that ZnO exhibits an average particle size of 10–20 nm (Supplementary Fig. 17a). No apparent Ru nanoparticles or clusters can be observed over 0.5Ru-ZnO, while obvious small dark dots can be observed over 2Ru-ZnO (Supplementary Fig. 17). The interplanar lattice spacing of 0.26 nm precisely corresponds to the (002) plane of ZnO (Supplementary Fig. 18). High-resolution TEM and scanning TEM (STEM) images also depict no discernible Ru species on 0.5Ru-ZnO, yet distinct 1–2 nm dark dots are observed on 2Ru-ZnO (Fig. 2d,e and Supplementary Fig. 19). Energy dispersive spectrometry mapping in Fig. 2f shows that Zn and Ru elements are uniformly dispersed over 0.5Ru-ZnO. Supplementary Fig. 20 shows that the weight percentage of Ru is 0.43 wt%. Aberration-corrected high-angle annular dark field STEM (HAADF-STEM) images were captured to further investigate Ru species over 0.5Ru-ZnO. Distinct bright spots were observed (Fig. 2g and Supplementary Fig. 21), and no obvious dimer structures or clusters were detected, suggesting that Ru is very likely dispersed in a monatomic state. Ru K-edge X-ray absorption near-edge structure (XANES) spectra and extended X-ray absorption fine structure (EXAFS) spectra were measured to investigate the coordination environment of 0.5Ru-ZnO. The Ru K-edge XANES spectra of 0.5Ru-ZnO show the oxidation state of Ru as between those of RuO₂ and metallic Ru foil and closer to the former (Fig. 2h), indicative of Ru species in a partially oxidized state on the ZnO support. Fourier-transformed EXAFS at the Ru K-edge does not present a signal corresponding to Ru–Ru bonding (Fig. 2i), indicating that the atomically dispersed Ru are stabilized by the O atoms of 0.5Ru-ZnO. The coordination environment of Ru was delineated through curve-fitting analysis of the EXAFS spectra (Supplementary Fig. 22) and is quantitatively summarized in Supplementary Table 4. The curve-fitting results of 0.5Ru-ZnO elucidate a pronounced peak at a radial distance of 2.006 Å, with a coordination number of 4.6, attributable to the Ru–O bonding interaction, which originates from the backscattering between atomically dispersed Ru centres and the surrounding O atoms of the substrate. From these observations, Ru is dispersed as single atoms with a chemical state of Ru⁴⁺ in the low-Ru-loading-amount sample (0.5Ru-ZnO) and as nanoparticles in the high-Ru-concentration sample (2Ru-ZnO). These findings align with recent studies on other metal oxides loaded with single atoms^{16,25}.

Mechanism of methane oxidation

Electrochemical characterizations were used to investigate O₂ reduction and methane oxidation involved in methane oxidation by O₂. A more negative current was achieved over 0.5Ru-ZnO than over ZnO (Fig. 3a), suggesting that Ru is an electron acceptor and promotes the

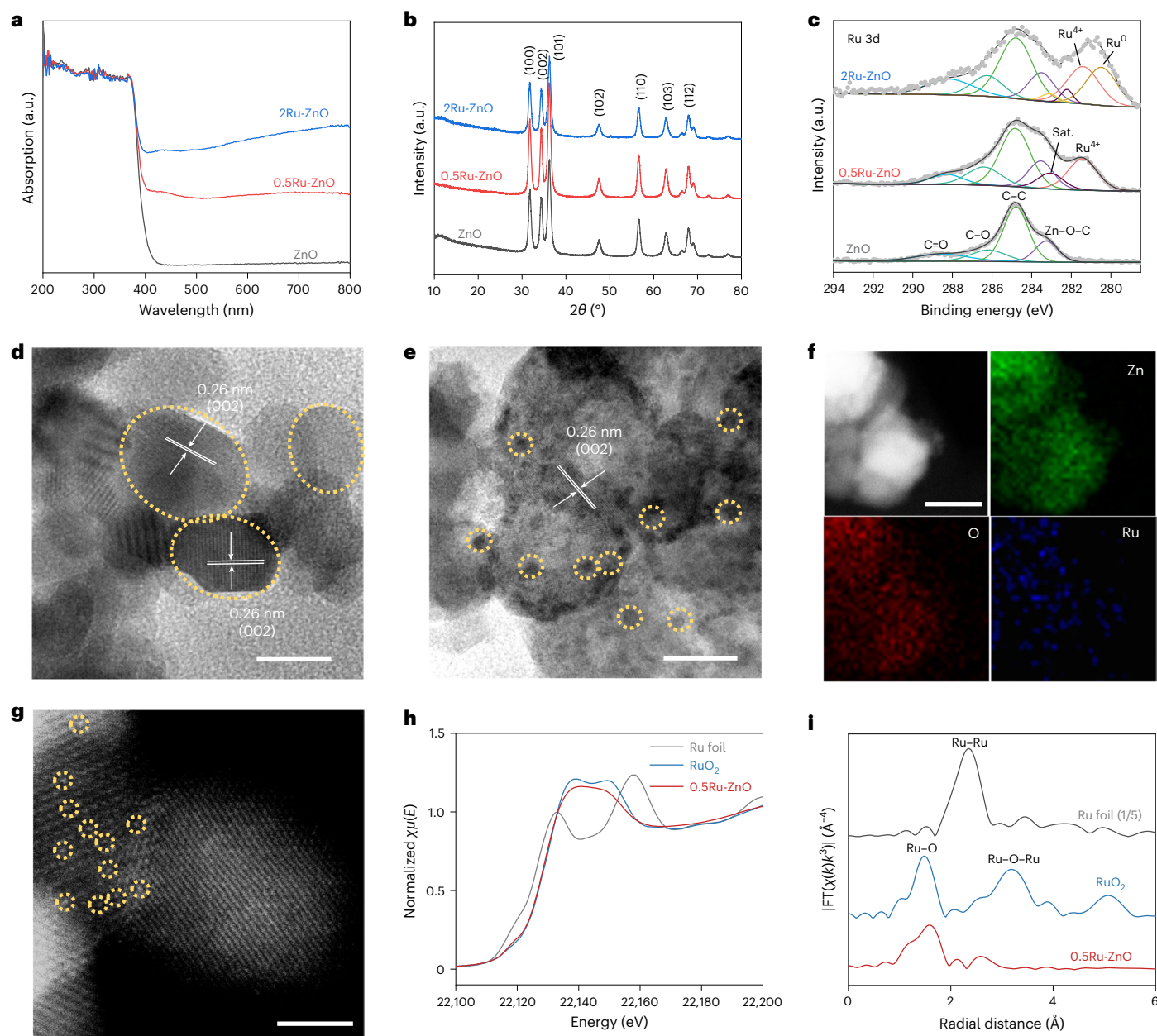


Fig. 2 | Characterization of the photocatalysts. **a, b**, UV-Vis spectra (**a**) and XRD patterns (**b**) of ZnO, 0.5Ru-ZnO and 2Ru-ZnO. **c**, Ru 3d and C 1s high-resolution XPS spectra of ZnO, 0.5Ru-ZnO and 2Ru-ZnO. Sat., satellite peak. **d, e**, High-resolution TEM images of 0.5Ru-ZnO (**d**) and 2Ru-ZnO (**e**). The yellow circles in **d** highlight the ZnO particles and in **e** highlight the Ru nanoparticles. **f**, The

element mappings of 0.5Ru-ZnO. Scale bars in **d–f**, 10 nm. **g**, HAADF-STEM image of 0.5Ru-ZnO. Scale bar, 2 nm. The yellow circles highlight Ru single atom sites. **h**, Normalized Ru K-edge XANES spectra of 0.5Ru-ZnO with Ru foil and RuO₂ as references. **i**, Fourier transform (FT) magnitudes of Ru K-edge EXAFS spectra in R space of 0.5Ru-ZnO and references.

oxygen reduction reaction. Moreover, 0.5Ru-ZnO exhibits a lower photocurrent density for methane oxidation than that of ZnO under a bias of 0.6 V versus reversible hydrogen electrode (RHE) in the CH₄-saturated electrolyte (Fig. 3b). This is because Ru serves as an electron acceptor and competes with the small bias, thus reducing the electron transfer to the counter electrode via the external circuit (Supplementary Fig. 23).

To obtain more insights into the role of Ru in charge transfer and recombination, we used photoluminescence (PL) spectroscopy. The PL peak of Ru-ZnO is substantially diminished compared with that of ZnO, suggesting a notable reduction in the charge recombination (Fig. 3c and Supplementary Fig. 24). In situ photo-induced absorption (PIA) spectroscopy was employed to delve deeply into the charge transfer processes. An in situ ultraviolet–visible–near-infrared diffuse reflectance spectroscopy (UV-Vis–NIRDRS) system was developed to

measure the reflectance of the photocatalyst under various lighting conditions and reaction atmospheres²⁶. Essentially, a constant 365 nm LED light functions as a ‘pump’ light, triggering continuous electron transition from the valance to the conduction band of ZnO, thus creating free carriers. Photons from the probe lamp are absorbed by these free carriers, exciting electrons to higher energy states²⁷. Through an analysis of the probe light absorption under dark (ground state) and light (excited state), PIA can be calculated by the following equation:

$$\Delta\text{Abs} = \frac{R_{\text{dark}} - R_{\text{light}}}{R_{\text{dark}}} \times 100\% \quad (1)$$

The calculated PIA spectrum shows absorption from 1,000 nm to 2,700 nm under Ar (Fig. 3d and Supplementary Fig. 25), which is

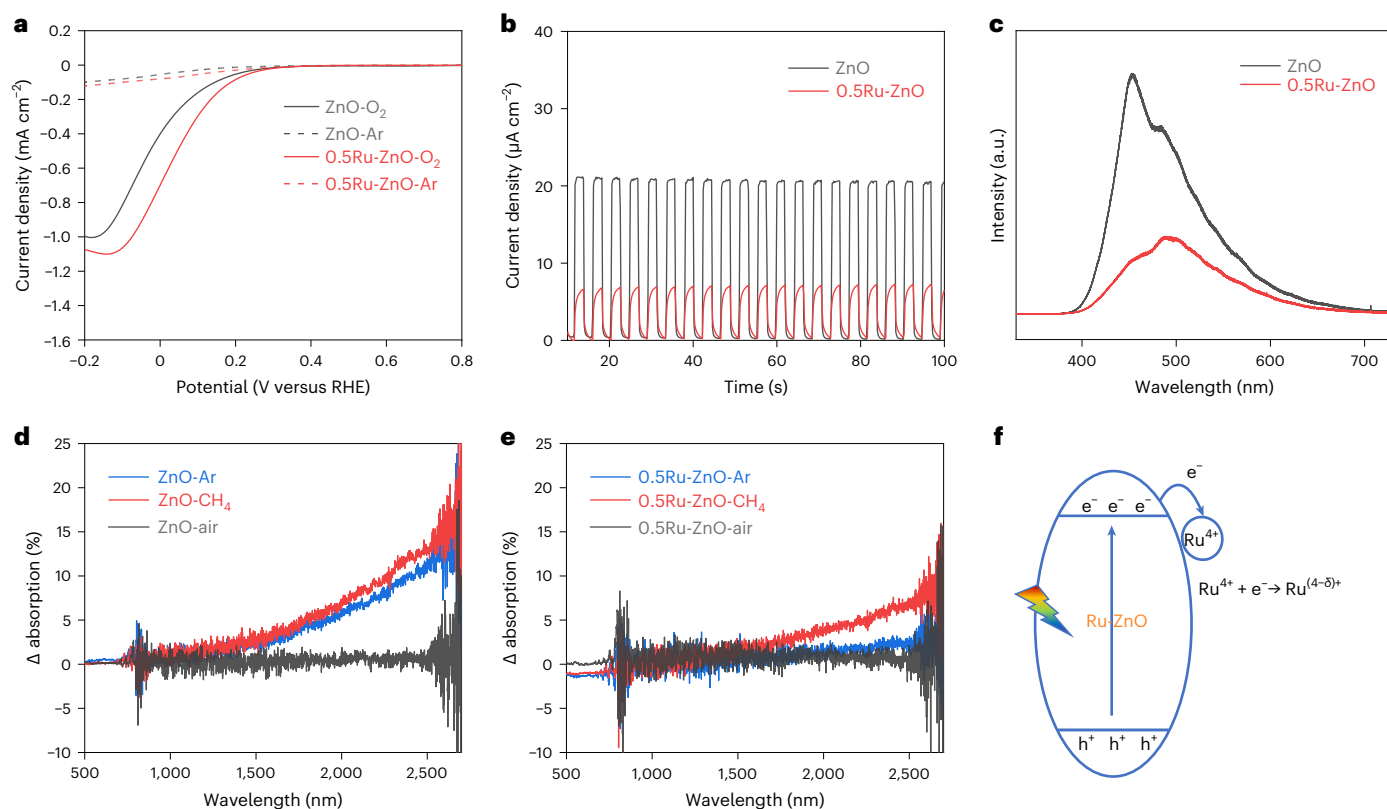


Fig. 3 | Pathways of charge transfer. **a, b**, Electrochemical oxygen reduction curves (**a**) and transient photocurrent density curves (**b**) of ZnO and 0.5Ru-ZnO with a bias of 0.6 V versus RHE. **c**, PL spectra of ZnO and 0.5Ru-ZnO. **d, e**, Photo-induced light absorption of ZnO (**d**) and 0.5Ru-ZnO (**e**) in Ar, CH₄ and air. **f**, Schematic illustration of the charge generation and transfer in 0.5Ru-ZnO.

attributed to free carrier absorption either in the conduction band or in the valence band of ZnO (ref. 27). The PIA of ZnO is quenched in air, attributable to the notable electron scavenging capacity of oxygen. The excited electrons in the conduction band are quickly consumed by oxygen, leaving less observable free carrier absorption. This supports the premise that the PIA of ZnO from 1,000 nm to 2,700 nm under Ar results from the excited electrons in the conduction band^{4,28}. Upon the introduction of methane, a marginal increase in the PIA spectrum is noticeable compared with that in Ar, indicating that methane is a hole acceptor, allowing for more excited electrons in the conduction band. Following this, we explored the PIA of 0.5Ru-ZnO in an Ar environment to investigate the charge transfer between Ru and ZnO (Fig. 3e). In comparison with the PIA of ZnO, 0.5Ru-ZnO displayed a pronounced decrease, mirroring the phenomenon observed when air was introduced. This implies that Ru is capable of quenching the excited electrons in the conduction band of ZnO. The PIA absorption of 0.5Ru-ZnO under a methane atmosphere exhibited similar outcomes as ZnO. Ru therefore acts as an electron acceptor. The photogenerated charge transfer process of 0.5Ru-ZnO is illustrated schematically in Fig. 3f.

The in situ electron paramagnetic resonance (EPR) spin-trapping technique was employed to investigate the mechanism of oxygen reduction, using 5,5-dimethyl-1-pyrroline-*N*-oxide (DMPO) as a spin trap¹⁵. 0.5Ru-ZnO generates more •OOH than ZnO (Fig. 4a), which is attributed to the superior separation efficiency of photoexcited carriers by the electron acceptor of Ru. However, an increase in Ru loading leads to a substantial drop in •OOH production due to the strong light scattering of Ru nanoparticles²⁹. To quantify the concentration of •OOH radicals, we employed nitroblue tetrazolium (NBT) as a scavenger of superoxide radicals³⁰. Pristine ZnO manifested a first-order kinetic constant of 0.035 min⁻¹, whereas 0.5Ru-ZnO exhibited a higher value of 0.058 min⁻¹ (Supplementary Fig. 26), which is consistent with the EPR

results. The generation of •OH radicals was also analysed. 0.5Ru-ZnO produced the highest quantity of •OH, while 2Ru-ZnO generated even lower amounts than the pristine ZnO (Fig. 4b). In the meantime, the 7-hydroxy coumarin fluorescence signal at 454 nm also confirms that 0.5Ru-ZnO promotes the production of •OH, while 2Ru-ZnO produces a substantially lower amount (Supplementary Fig. 27), which is also due to the scattering effect of Ru nanoparticles²⁹. To investigate whether methane is activated by photo-induced holes or •OH, we conducted control experiments with different solvents (Supplementary Figs. 28 and 29), together with adding sacrificial agents for •OH and h⁺ (Supplementary Fig. 30)^{31–33}. All these clearly indicate the importance of •OH radicals in methane activation and high-value chemical synthesis, which should be produced by water oxidation by photoholes.

To confirm the oxygen source of HCHO, we conducted isotope experiments of methane oxidation over 0.5Ru-ZnO using ¹⁸O₂ or H₂¹⁸O. The oxygen in HCHO is mainly from H₂O rather than O₂ (Fig. 4c), and the oxygen in HCHO produced by 0.5Au-ZnO and 2Ru-ZnO is also from H₂O rather than O₂ (Supplementary Figs. 31a and 32a). These results are consistent with previous isotopic experiments on HCHO produced by single-atom Cu-modified WO₃ and ethane oxidation to acetaldehyde^{17,34}. In contrast, the oxygen in CH₃OH is from O₂, as evidenced by the isotopic results over 0.5Au-ZnO and 2Ru-ZnO (Supplementary Figs. 31b and 32b), which is consistent with the isotopic experiments on CH₃OH produced by Au-ZnO and Au_{NPs}-In₂O₃ (refs. 15,16). These findings suggest that HCHO is produced by another reaction pathway rather than the oxidation of CH₃OH.

In situ diffuse reflectance infrared Fourier transform spectroscopy (DRIFTS) was employed to understand the photocatalytic oxidation process of methane. The peak at 1,304 cm⁻¹ is ascribed to CH₄ (Fig. 4d). 0.5Ru-ZnO shows a band at 2,854 cm⁻¹, which is associated with the C–H stretching vibration of adsorbed •CH₃ species (Fig. 4e)³⁵. The intensity

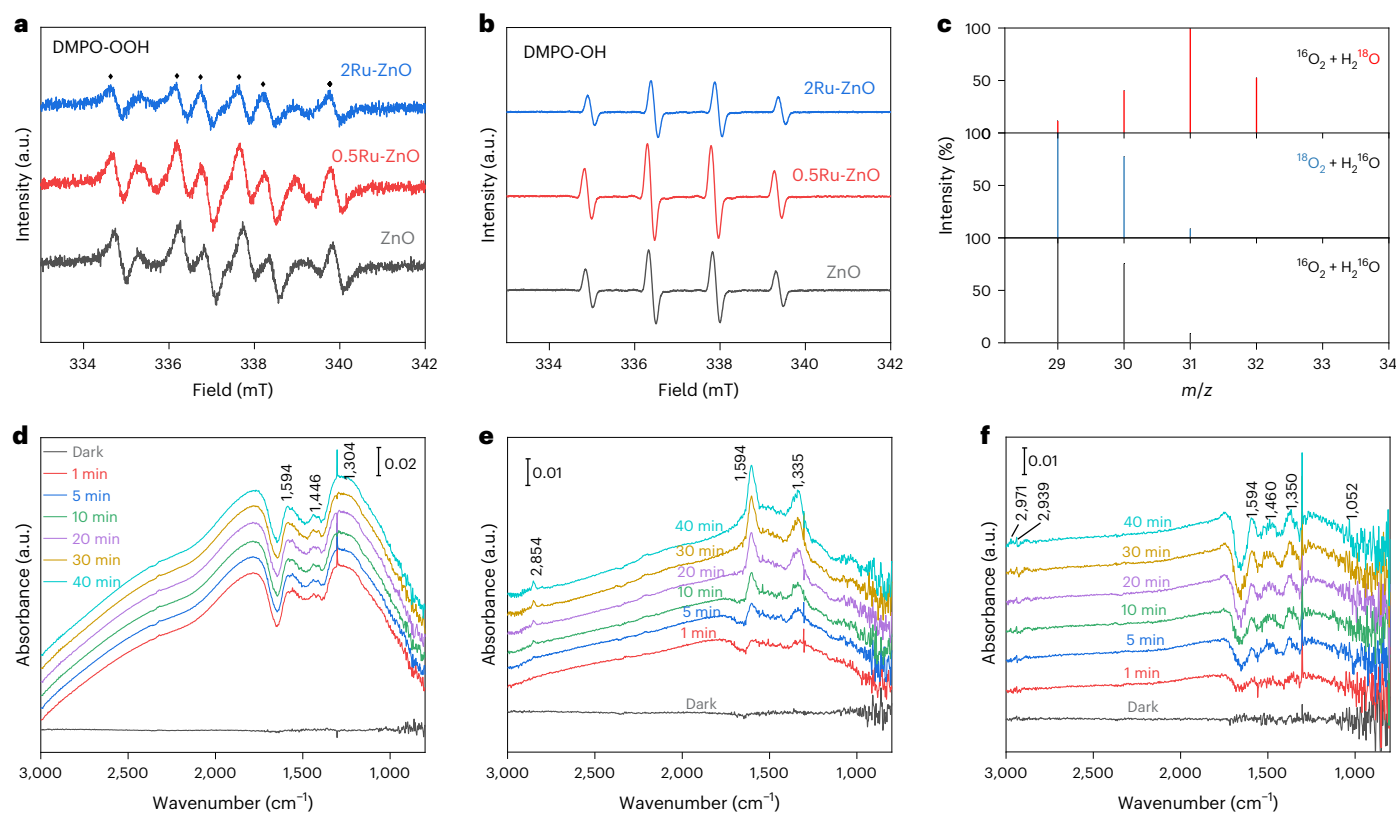


Fig. 4 | Mechanism of photocatalytic methane oxidation. a, EPR spectra of ZnO, 0.5Ru-ZnO and 2Ru-ZnO for the detection of \bullet OOH radicals in air-saturated methanol solution under light irradiation. **b**, EPR spectra of ZnO, 0.5Ru-ZnO and 2Ru-ZnO for the detection of \bullet OH radicals. **c**, GC-MS spectra of HCHO produced

by CH_4 oxidation over 0.5Ru-ZnO with $^{16}\text{O}_2 + \text{H}_2^{18}\text{O}$, $^{18}\text{O}_2 + \text{H}_2^{16}\text{O}$ or $^{16}\text{O}_2 + \text{H}_2^{16}\text{O}$. **d-f**, In situ DRIFT spectra for photocatalytic CH_4 conversion over ZnO (**d**), 0.5Ru-ZnO (**e**) and 2Ru-ZnO (**f**) in the presence of CH_4 , O_2 and water vapour.

of this band increases with prolonged irradiation time. However, this feature was not observed over both ZnO and 2Ru-ZnO, strongly indicating the high methane activation efficiency of 0.5Ru-ZnO. The peaks at 1,335/1,350 cm^{-1} , attributed to the vibration of adsorbed CH_3OOH species^{36–38}, were observable in 0.5Ru-ZnO but notably weaker in 2Ru-ZnO. Furthermore, vibrational peaks at 1,052 cm^{-1} , 2,939 cm^{-1} and 2,971 cm^{-1} , associated with methoxy and C–H stretching vibrations in CH_3OH (refs. 39,40), are uniquely present in 2Ru-ZnO and 0.5Au-ZnO (Fig. 4f and Supplementary Fig. 33). This implies that methanol production is favourable over 2Ru-ZnO, aligning with the product selectivity of 0.5Ru-ZnO and 2Ru-ZnO in catalytic methane oxidation. Two peaks at 1,446/1,460 cm^{-1} and 1,594 cm^{-1} are attributed to $\text{HCOO}\bullet$ species³⁵. The peak area of this band keeps increasing with time over ZnO, 0.5Ru-ZnO and 2Ru-ZnO, indicating that the consumption of $\text{HCOO}\bullet$ is much slower than its formation on the surface of the catalyst. The accumulation of $\text{HCOO}\bullet$ prevents further oxidation of $\text{HCOO}\bullet$ to CO_2 , consistent with the high selectivity of oxygenates over all catalysts⁴¹.

To fully understand the reaction process of HCHO production from methane by 0.5Ru-ZnO, it is necessary to consider both photocatalysis and phonon energy. The methane oxidation performance by photocatalysis, thermocatalysis and photon–phonon-driven cascade catalysis is compared in Fig. 5a. Only a trace amount of HCHO was produced by thermocatalysis at 150 °C. A notable production rate of CH_3OOH , accompanied by a modest quantity of HCHO, was observed by photocatalysis at 30 °C. CH_3OOH is stable at room temperature (Supplementary Table 5). In contrast, the cascade of photocatalysis and phonon-driven decomposition generates a substantial quantity of HCHO (401.5 $\mu\text{mol h}^{-1}$) with a high selectivity (>90%), highlighting the efficacy of phonon input in promoting the product yield. Compared with photocatalysis, the HCHO yield by photon–phonon-driven

cascade catalysis increased by nearly 30-fold, and the selectivity improved almost eightfold. Moreover, CH_3OOH , which is produced by the oxidation of methane through photocatalysis at 30 °C, is subsequently subjected to 150 °C without light irradiation (Fig. 5b). The secondary step leads to all CH_3OOH molecules being transformed to CH_3OH , HCHO and CO_2 , with HCHO as the primary product (~80%). The transformation of CH_3OOH over ZnO or in the absence of the catalyst shows similar results (Supplementary Figs. 34 and 35), suggesting that CH_3OOH conversion to HCHO is a phonon-driven decomposition step.

To explain the isotopic result and the high selectivity of CH_3OOH over 0.5Ru-ZnO, we undertook theoretical modelling, and we propose the following reaction pathways (Fig. 5c,d and Supplementary Fig. 36). Upon photon irradiation, excited electrons in the conduction band of ZnO are transferred to Ru^{4+} , reducing it to $\text{Ru}^{(4-\delta)+}$. $\text{Ru}^{(4-\delta)+}$ then reduces the adsorbed O_2 to H_2O . Methane is first activated by \bullet OH radicals from water oxidation to produce adsorbed $\bullet\text{CH}_3$. The reaction energy barrier of $\bullet\text{CH}_3$ over $\text{Ru}_{\text{SA}}\text{-ZnO}$ is lower than that over $\text{Ru}_{\text{NPS}}\text{-ZnO}$. Following this, the adsorbed $\bullet\text{CH}_3$ reacts with \bullet OH species produced from the oxidation of adsorbed water to form adsorbed $\bullet\text{CH}_3\text{OH}$ species. The adsorption energy of $\bullet\text{CH}_3\text{OH}$ species on $\text{Ru}_{\text{SA}}\text{-ZnO}$ (–1.30 eV) is lower than that on $\text{Ru}_{\text{NPS}}\text{-ZnO}$ (–1.42 eV), which results in a lower reaction energy for the further reaction of $\bullet\text{CH}_3\text{OH}$ species with \bullet OH to form $\bullet\text{CH}_3\text{OOH}$ on $\text{Ru}_{\text{SA}}\text{-ZnO}$. CH_3OOH is therefore formed more easily on $\text{Ru}_{\text{SA}}\text{-ZnO}$, indicating that CH_3OOH is the main intermediate on $\text{Ru}_{\text{SA}}\text{-ZnO}$, while there is less CH_3OOH formed on $\text{Ru}_{\text{NPS}}\text{-ZnO}$. Subsequently, the adsorbed $\bullet\text{CH}_3\text{OOH}$ desorbs to form CH_3OOH or further undergoes dehydration to form the adsorbed $\bullet\text{HCHO}$, which then desorbs in the form of HCHO. In addition, Ru with a high weight percentage (2Ru) and other metals (Au, Pd, Pt and Ag) were loaded onto ZnO in the form of nanoparticles (Supplementary Fig. 37), which probably creates a new

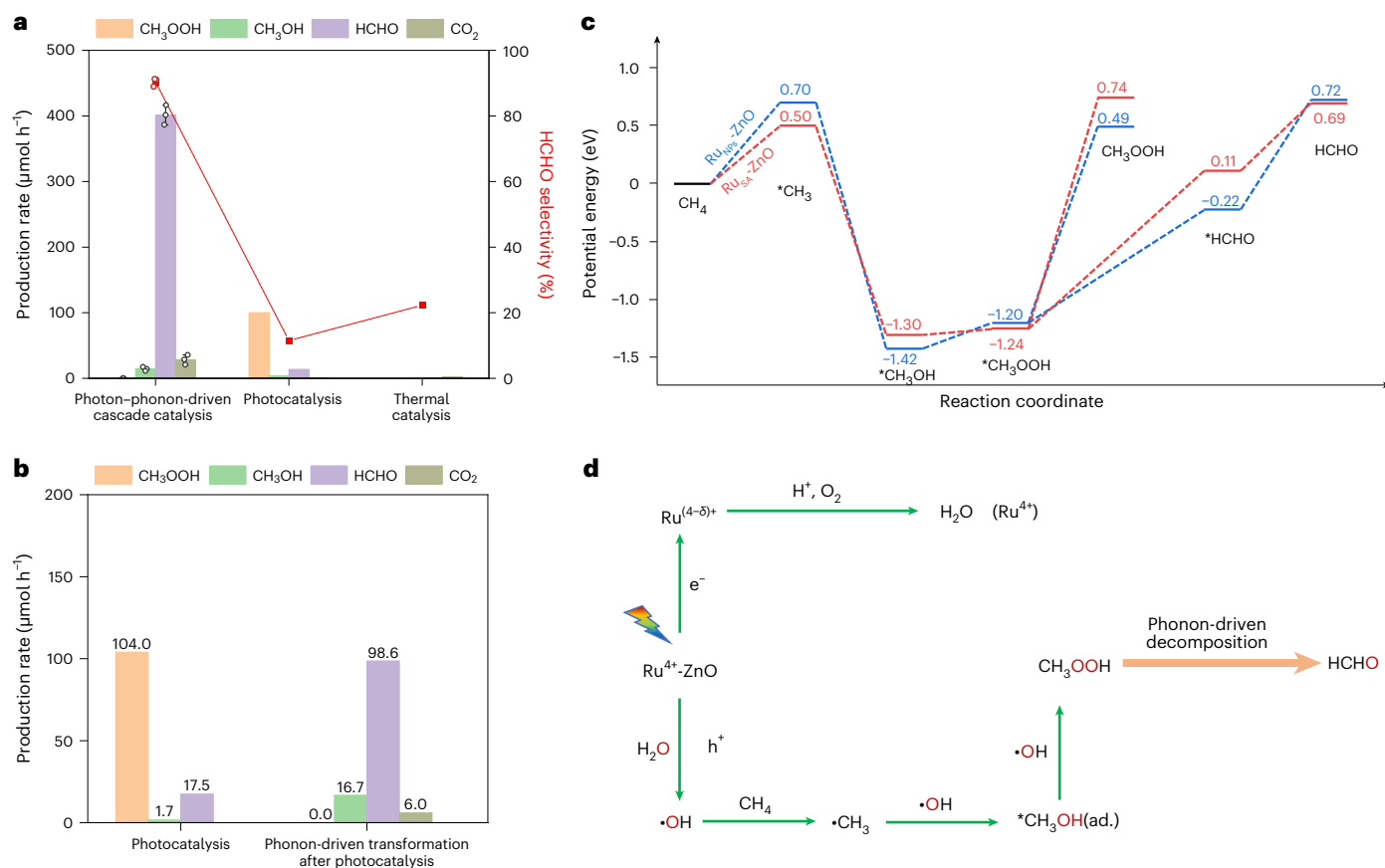


Fig. 5 | Reaction pathways. a, Methane oxidation performance by photocatalysis, thermocatalysis and photon-phonon-driven cascade catalysis. The error bars were obtained from three independent reactions. The data are presented as mean values \pm standard error of the mean. **b**, Photocatalytic methane conversion over 0.5Ru-ZnO first at 30 °C under light irradiation and then kept at 150 °C in the dark for 1 h. The following reaction conditions were used: 10 mg photocatalysts, 180 ml water, 20 bar CH₄, 0.75 bar O₂, 365 nm LED

(75 mW cm⁻², illumination area of 12.56 cm²)/without light, 1 h reaction. **c**, Reaction path for methane oxidation over Ru_{5a}-ZnO (red curve) and Ru-nanoparticle-decorated ZnO (Ru_{nps}-ZnO, blue curve). The potential energy (eV) denotes the energy associated with different intermediates in the reaction. **d**, The proposed reaction pathways of photon-phonon-driven cascade catalysis for methane oxidation to HCHO. ad., adsorbed.

reaction pathway for CH₃OH production (Supplementary Fig. 38). It is proposed that photogenerated holes oxidize H₂O to produce •OH, which then oxidizes CH₄ to •CH₃. In parallel, O₂ is reduced by photoelectrons to generate H₂O₂ and then •OH. CH₃OH is next produced from the combination of •CH₃ and •OH radicals on the nanoparticle cocatalysts.

Discussion

In summary, this work reports a benchmark yield of HCHO from methane oxidation by photon-phonon-driven cascade catalysis. With intact consecutive photocatalysis and thermodecomposition, an HCHO production rate of 401.5 μmol h⁻¹ with a selectivity of >90% was achieved over Ru_{5a}-ZnO operated at 150 °C. Mechanism studies prove that Ru_{5a} acts as an electron acceptor and improves charge separation in photocatalytic oxygen reduction. Oxygen isotopic experiments and theoretical modelling indicate that methane reacts with H₂O to selectively produce CH₃OOH over Ru_{5a}-ZnO via photocatalysis. The phonon-driven step readily transforms CH₃OOH to HCHO, resulting in an increase in the yield of HCHO by nearly 30-fold, while the selectivity is improved by almost eightfold. By combining the high selectivity of photocatalysis and the high reactivity of thermodecomposition, this work realizes highly efficient and selective oxidation of methane to HCHO under mild conditions, potentially reducing the carbon footprint related to HCHO production from methane. The current reaction pathway, characterized by minimized energy consumption and high efficiency, offers a promising approach for the sustainable conversion of methane.

Methods

Chemicals and materials

All reagents were commercially available and were used without any purification. The gases methane (CP grade), oxygen and argon (zero grade) were sourced from BOC. Zinc nitrate hexahydrate (98%, extra pure), oxalic acid (98%, anhydrous) and potassium iodide (≥99%, for analysis) were acquired from Acros Organics. Potassium tetrachloropalladate (98%), gold(III) chloride trihydrate (≥99.9% trace metals basis), chloroplatinic acid hexahydrate, silver nitrate, sodium borohydride (≥98.0%) and coumarin were obtained from Sigma Aldrich. Ruthenium(III) chloride hydrate (99.9%, Ru 38% min.) was purchased from Alfa Aesar. NBT (>99%) was received from Apollo Scientific. Ammonium molybdate 4H₂O (Analytical Reagent, >99%) was obtained from SLS SELECT. Ethanol absolute (HPLC grade) was sourced from Fisher Chemical.

Materials synthesis

The ZnO nanoparticles were synthesized via the precipitation method with a small modification of the procedure outlined in the literature⁴². An identical molar concentration of 0.025 moles of zinc nitrate (Zn(NO₃)₂) and oxalic acid were separately dissolved in 500 ml of deionized water. The oxalic acid solution was then gradually introduced into the zinc nitrate solution in a dropwise fashion using a separating funnel, resulting in the precipitation of zinc oxalate. Following precipitation, these zinc oxalate precipitates were dried in an oven at 60 °C and were subsequently calcinated in air at 350 °C for 6 h.

Ru was deposited onto ZnO following a chemical reduction method. In a standard procedure, 200 mg ZnO nanopowder was dispersed in 100 ml of deionized water and agitated for 20 min. A designated measure of ruthenium(III) chloride hydrate solution (0.5 mg ml⁻¹ relative to metallic Ru) was then added drop by drop and the mixture was stirred for an extra 60 min. In the ensuing step, 2 ml NaBH₄ solution (0.1 M) was introduced gradually into the above-formulated suspension. After stirring for 60 min, the product was washed by centrifugation with a centrifugal force of ~900 *g* and dried at 60 °C. Pd, Au, Pt and Ag were deposited onto ZnO using the same method with the corresponding metal precursors.

Characterizations

XRD was performed using a Stoe STADI-P diffractometer, equipped with a Cu K α source ($\lambda = 1.5418 \text{ \AA}$, scanned from 10 to 80°). Ultraviolet–visible diffuse reflectance spectroscopy (UV–Vis DRS) measurements were conducted employing a Shimadzu UV-2550 spectrophotometer, which is equipped with an integrating sphere. The reflectance values were directly converted to absorption using the Kubelka–Munk equation. The XPS analysis was carried out using a Thermo Scientific XPS machine, outfitted with an Al K α source emitting at a photon energy (h ν) of 1,486.6 eV. TEM analysis was performed using a JEOL 2010 instrument. Aberration-corrected HAADF-STEM was performed with a Cs-corrected JEM ARM200CF microscope operated at 200 kV using an angle annular detector with a collection angle of 40–160 mrad. In terms of PL, data were gathered from 330 nm to 800 nm using a Renishaw InVia spectroscopy, with a 325 nm laser as the excitation source. The X-ray absorption fine structure spectra (Ru K-edge) were collected at the BL14W beamline in the Shanghai Synchrotron Radiation Facility (SSRF). The storage ring of the SSRF was operated at 3.5 GeV with a stable current of 200 mA. Using an Si (111) double-crystal monochromator, the data collection was carried out in fluorescence mode using an SDD detector. All spectra were collected in ambient conditions.

In situ UV–Vis–NIR DRS measurement

The Agilent Cary 5000 UV–Vis–NIR spectrometer was used to conduct in situ measurements of charge transfer behaviour. It was fitted with a Praying Mantis diffuse reflection accessory and a Harrick cell, which guided the beam path and controlled the sample setting. The triple windows of the Harrick cell, crafted from crystal quartz, are transparent to UV, visible and near-infrared light. Two of these windows paved the way for measurement light, while the third facilitated the excitation light. To act as the irradiation source, a 365 nm UV LED paired with a 365 nm bandpass filter was employed to provide pure 365 nm irradiation. A 450-nm-long pass filter ($\lambda > 450 \text{ nm}$) installed before the spectrometer's detector was used to prevent interference from the scattering light of the LED source.

Every test involved loading 50 mg of catalyst into the sample holder of the Harrick cell. A flat measurement surface was set up using a metal spatula. After that, Ar, air or methane purged the Harrick cell for 20 min at a flow rate of 100 ml min⁻¹. The cell was then sealed for the measurement process. Reflectance spectra spanning from 500 to 2,700 nm were recorded both in the dark and under LED irradiation. Each test was run three times, and the resultant average reflectance values served as the analysis basis.

Electrochemical measurement

The photoelectrodes were fabricated using a spin-coating method. Typically, 20 mg of photocatalyst was dispersed in 2 ml of ethanol and subsequently sonicated for 60 min. Fluorine-doped tin oxide (FTO) glass (2 cm \times 2 cm) was used as the substrate. 80 μ l of the suspension was deposited onto FTO glass and rotated at a speed of 500 rpm for 30 s. After the spin-coating process, the electrode was transferred to a hotplate and dried at 100 °C for 15 min.

All electrochemical tests were conducted within a three-electrode cell using a 0.5 M Na₂SO₄ solution as the electrolyte. The FTO glass

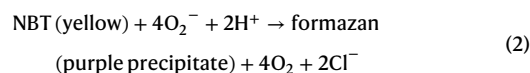
coated with the photocatalyst served as the working electrode, while a Pt plate and an Ag/AgCl electrode immersed in a saturated KCl solution functioned as the counter electrode and reference electrode, respectively. The oxygen reduction reaction was carried out within a voltage window ranging from 1 to -0.2 V versus RHE at a scan rate of 10 mV s⁻¹. For the photocurrent measurement, a bias potential of 0.6 V versus RHE was applied. A 150 W xenon lamp was used as the light source, with the light being chopped every 2 s.

EPR measurement

EPR spectroscopy analysis was conducted on a Bruker E580 X-band spectrometer, incorporating DMPO as the radical trapping agent. For the superoxide (O₂⁻) radical test, 4 mg of photocatalyst was dispersed in 4 ml of methanol solution with 50 mM DMPO. The mixture was then illuminated using a 365 nm LED for 5 min in an air atmosphere while being stirred. After the reaction, 0.5 ml of the mixture was quickly transferred to a quartz tube for testing. The EPR testing was carried out at ambient temperature, with a modulation frequency of 100 kHz, a microwave frequency of 9.46 GHz, a sweep time of 60 s, a microwave output of 10 mW and a scan from 330 to 345 mT. The procedure carried out in dark conditions was identical to the above but without the UV irradiation. The procedure for the \bullet OH radical test was similar to that of the \bullet OOH radical test except that the solution was composed of water containing 10 mM DMPO.

Quantitative analysis of superoxide radicals

NBT, a well-known superoxide radical scavenger, was used as the probing molecule to quantify hydroperoxyl radicals³⁰. NBT reacts with superoxide radicals (reducing the nitro group) to produce formazan, which is a purple-coloured precipitate. The reaction can be summarized as follows:



Conventionally, a 10 mg sample of the photocatalyst was amalgamated with 150 ml of 0.04 mM NBT solution (10% ethanol in water), followed by stirring in darkness for 30 min. As hydroxyl radicals can also cause the reduction of NBT to formazan, ethanol was added as a hydroxyl radical scavenger. The solution was subjected to 365 nm LED irradiation in an air atmosphere, and 5 ml of reactant solution was collected at regular intervals of 5 min. Following filtration, the UV–Vis spectra of the samples were then recorded using the Shimadzu UV-2550 spectrofluorometer. The absorption at 259 nm was used to indicate the remaining NBT.

Quantitative analysis of hydroxyl radicals

Coumarin was employed as a probe to quantify \bullet OH through the generation of 7-hydroxy coumarin. Typically, 10 mg of photocatalyst was uniformly dispersed in a 120 ml solution of 0.5 mM coumarin with or without ethanol. The suspension was then subjected to a light source (365 nm LED) for 1 h. 3 ml of the suspension was sampled and subsequently filtered. The PL intensity of the resulting 7-hydroxy coumarin in the solution was measured using the Fluorolog spectrofluorometer under a 335 nm excitation.

In situ DRIFTS measurement

In situ DRIFTS was conducted using a Nicolet iS50 FTIR Spectrometer with an MCT detector, supplemented with a Harrick cell and a Praying Mantis accessory. Each spectrum was collected by taking an average of 128 scans, maintaining a resolution of 4 cm⁻¹. The cell was equipped with two ZnSe windows designated for IR transmission and a quartz window reserved for UV irradiation. For each test, 50 mg of photocatalyst was positioned in the sample holder of the cell with a flat surface. Subsequently, the cell underwent a 30 min purge process

in the dark with water-vapour-saturated CH₄ and O₂ mixing gas (in a ratio of CH₄/O₂ = 20:0.75). Once purged, the cell was engaged in an airtight seal and nested into the Praying Mantis accessory. The entirety of this assembly was then affixed within the spectrometer. A 'dark' reference baseline was obtained by cataloguing the photocatalyst's signal in the reaction atmosphere under dark conditions. During the measurement, the catalyst was exposed to radiation from a 365 nm LED. The spectral data were recorded at distinct irradiation durations of 1, 5, 10, 20, 30 and 40 min.

Methane oxidation reaction

Photocatalytic methane oxidation reactions were undertaken within a 230 ml homemade batch reactor, specifically designed with an integrated quartz window for light irradiation. In a typical reaction, 10 mg of photocatalyst was dispersed into 180 ml of water and sonicated for 10 min. Upon completion, the resultant suspension was transferred to the batch reactor. The reactor was subsequently purged with Ar for 15 min to evacuate air from the headspace. Following this, the reactor was pressurized at room temperature (~25 °C) with pure O₂ at 0.75 bar and pure CH₄ at 20 bar. The reactor was then placed within a heating mantle, and its temperature was ramped up to 150 °C while it was stirred at 800 rpm. A thermocouple was strategically positioned within the solution for the precise detection of the temperature of the liquid solution. Once a stable temperature was achieved, the reactor was exposed to irradiation through a 100 W 365 nm LED light (sourced from Beijing Perfect Light, model PLS-LED 100C). The light intensity following the quartz window was 75 mW cm⁻², and the irradiation area was 12.56 cm².

After the reaction, the reactor was subjected to rapid cooling in a water bath until a temperature below 25 °C was achieved. Subsequently, the gaseous product released from the outlet was sampled by a GC syringe and injected into a GC (Varian 450), equipped with a TCD detector, a methanizer and an FID detector. The liquid product was filtered and collected for further analysis. The concentrations of CH₃OOH and CH₃OH within the liquid were accurately quantified using the 1H NMR spectrum (Bruker Avance Neo 700 MHz). This was undertaken by mixing 0.5 ml of liquid product with 0.1 ml of D₂O containing 0.768 μmol ml⁻¹ dimethyl sulfoxide (Wako, 99.99%) as an internal standard. Calibration curves were configured by plotting the standard concentrations of methanol with the area ratio between methanol to dimethyl sulfoxide (Supplementary Fig. 2). Given the identical proton count within the methyl groups of both the CH₃OH and CH₃OOH molecules, the calibration curve employed for the quantitative analysis of CH₃OOH serves equivalently for the quantification of CH₃OH. The quantification of HCHO was performed using a colorimetric method¹⁵. Initially, 50 ml of reagent solution was prepared by the dissolution of 7.5 g of ammonium acetate, 0.15 ml of acetic acid and 0.1 ml of pentane-2,4-dione in water. Subsequently, a mixture was prepared by combining 0.5 ml of the liquid product, 2.0 ml of water and 0.5 ml of the reagent solution. This solution was conserved at room temperature overnight, and the concentration of HCHO was evaluated by analysing the absorption intensity at 412 nm via a UV-Vis absorption spectrometer. The concentration of HCHO was quantified using a standard curve, referenced in Supplementary Fig. 2. The product selectivity was calculated on the basis of observable products as the following:

$$\text{Selectivity of HCHO} = \frac{n_{\text{HCHO}}}{n_{\text{CH}_3\text{OOH}} + n_{\text{CH}_3\text{OH}} + n_{\text{HCHO}} + n_{\text{CO}} + n_{\text{CO}_2}} \times 100\% \quad (3)$$

where n represents the yield of products in a certain period.

For the cycling test, 10 mg of 0.5Ru-ZnO was used for photocatalytic methane oxidation under the optimized conditions. Seven cycles were conducted, and each cycle lasted 2 h. Between each cycle, liquid products and water were evaporated to preclude the loss of photocatalysts.

Isotopic experiments

For an oxygen source with isotopically labelled ¹⁸O₂, 10 mg of 0.5Ru-ZnO (2Ru-ZnO or 0.5Au-ZnO) was dispersed in 180 ml of H₂¹⁶O; then, the reactor was purged with Ar for 30 min and pressurized with 0.75 bar ¹⁸O₂ (97 atom % ¹⁸O, Sigma-Aldrich) and 20 bar CH₄. For the investigation of the oxygen source in the products using isotopically labelled H₂¹⁸O, 10 mg of 0.5Ru-ZnO was dispersed in 3 ml of H₂¹⁸O (97 atom % ¹⁸O, Sigma-Aldrich), and then the reactor was purged with Ar for 30 min and pressurized with 0.75 bar ¹⁶O₂ and 20 bar CH₄. After the temperature reached 150 °C, the reactor was illuminated by a 365 nm LED for 2 h. The as-produced HCHO was measured with a GC-MS (8890-5977, Agilent) equipped with an HP-PLOT Q column.

Density functional theory calculations

The Vienna Ab Initio Simulation Package was employed to perform all density functional theory calculations^{43,44}. The projector augmented wave method was used for the interaction between ionic cores and valence electrons, and the exchange-correlation energies were calculated via the generalized gradient approximation with the Perdew-Burke-Ernzerhof functional^{45,46}. The 4 × 4 supercell of ZnO (001) was selected to avoid the interaction between neighbouring slab models with five atomic layers, and a vacuum layer of 15 Å was added along the z axis direction. Monkhorst pack k -points of 3 × 3 × 1 were applied for all calculations to sample the Brillouin zones. An energy cutoff of 400 eV was used for the plane-wave basis set. The geometries were optimized with the self-consistent field and force convergence criteria set to 10⁻⁵ eV and 0.05 eV Å⁻¹, respectively.

Reporting summary

Further information on research design is available in the Nature Portfolio Reporting Summary linked to this article.

Data availability

All data supporting the findings of this study are available within the paper and its supplementary files. Source data are provided with this paper.

References

- Li, X., Wang, C. & Tang, J. Methane transformation by photocatalysis. *Nat. Rev. Mater.* **7**, 617–632 (2022).
- Bahmanpour, A. M., Hoadley, A. & Tanksale, A. Critical review and exergy analysis of formaldehyde production processes. *Rev. Chem. Eng.* **30**, 583–604 (2014).
- Malik, M. I., Abatzoglou, N. & Achouri, I. E. Methanol to formaldehyde: an overview of surface studies and performance of an iron molybdate catalyst. *Catalysts* **11**, 893 (2021).
- Wang, H. et al. High quantum efficiency of hydrogen production from methanol aqueous solution with PtCu-TiO₂ photocatalysts. *Nat. Mater.* **22**, 619–626 (2023).
- Kim, Y. et al. Redox-driven restructuring of lithium molybdenum oxide nanoclusters boosts the selective oxidation of methane. *Nano Energy* **82**, 105704 (2021).
- Kunkel, B., Kabelitz, A., Buzanich, A. G. & Wohrlab, S. Increasing the efficiency of optimized V-SBA-15 catalysts in the selective oxidation of methane to formaldehyde by artificial neural network modelling. *Catalysts* **10**, 1411 (2020).
- Akiyama, T., Sei, R. & Takenaka, S. Partial oxidation of methane to formaldehyde over copper-molybdenum complex oxide catalysts. *Catal. Sci. Technol.* **11**, 5273–5281 (2021).
- van Steen, E., Guo, J., Hytoolakhan Lal Mahomed, N., Leteba, G. M. & Mahlaba, S. V. L. Selective, aerobic oxidation of methane to formaldehyde over platinum—a perspective. *ChemCatChem* **15**, e202201238 (2023).
- Tian, J. et al. Direct conversion of methane to formaldehyde and CO on B₂O₃ catalysts. *Nat. Commun.* **11**, 5693 (2020).

- Matsuda, A., Tateno, H., Kamata, K. & Hara, M. Iron phosphate nanoparticle catalyst for direct oxidation of methane into formaldehyde: effect of surface redox and acid–base properties. *Catal. Sci. Technol.* **11**, 6987–6998 (2021).
- Shimura, K. & Fujitani, T. Effects of promoters on the performance of a VO_x/SiO₂ catalyst for the oxidation of methane to formaldehyde. *Appl. Catal. A* **577**, 44–51 (2019).
- Fan, Y. et al. Selective photocatalytic oxidation of methane by quantum-sized bismuth vanadate. *Nat. Sustain.* **4**, 509–515 (2021).
- Jiang, Y. et al. Elevating photooxidation of methane to formaldehyde via TiO₂ crystal phase engineering. *J. Am. Chem. Soc.* **144**, 15977–15987 (2022).
- Wei, S. et al. Aerobic oxidation of methane to formaldehyde mediated by crystal-O over gold modified tungsten trioxide via photocatalysis. *Appl. Catal. B* **283**, 119661 (2021).
- Song, H. et al. Direct and selective photocatalytic oxidation of CH₄ to oxygenates with O₂ on cocatalysts/ZnO at room temperature in water. *J. Am. Chem. Soc.* **141**, 20507–20515 (2019).
- Jiang, Y. et al. Enabling specific photocatalytic methane oxidation by controlling free radical type. *J. Am. Chem. Soc.* **145**, 2698–2707 (2023).
- Luo, L. et al. Nearly 100% selective and visible-light-driven methane conversion to formaldehyde via single-atom Cu and W⁵⁺. *Nat. Commun.* **14**, 2690 (2023).
- Song, H., Meng, X., Wang, Z.-J., Liu, H. & Ye, J. Solar-energy-mediated methane conversion. *Joule* **3**, 1606–1636 (2019).
- Nguyen, T. L. & Stanton, J. F. The reaction of HO₂ and CH₃O₂: CH₃OOH formed from the singlet electronic state surface. *Atmosphere* **13**, 1397 (2022).
- Zhang, X., He, S. Z., Chen, Z. M., Zhao, Y. & Hua, W. Methyl hydroperoxide (CH₃OOH) in urban, suburban and rural atmosphere: ambient concentration, budget, and contribution to the atmospheric oxidizing capacity. *Atmos. Chem. Phys.* **12**, 8951–8962 (2012).
- Matthews, J., Sinha, A. & Francisco, J. S. Unimolecular dissociation and thermochemistry of CH₃OOH. *J. Chem. Phys.* **122**, 221101 (2005).
- Jin, Z. et al. Hydrophobic zeolite modification for in situ peroxide formation in methane oxidation to methanol. *Science* **367**, 193–197 (2020).
- Mishra, D. K. et al. Carbon doped ZnO: synthesis, characterization and interpretation. *J. Magn. Magn. Mater.* **329**, 146–152 (2013).
- Wang, H., Li, X., Ruan, Q. & Tang, J. Ru and RuO_x decorated carbon nitride for efficient ammonia photosynthesis. *Nanoscale* **12**, 12329–12335 (2020).
- Luo, L. et al. Synergy of Pd atoms and oxygen vacancies on In₂O₃ for methane conversion under visible light. *Nat. Commun.* **13**, 2930 (2022).
- Tang, J., Durrant, J. R. & Klug, D. R. Mechanism of photocatalytic water splitting in TiO₂: reaction of water with photoholes, importance of charge carrier dynamics, and evidence for four-hole chemistry. *J. Am. Chem. Soc.* **130**, 13885–13891 (2008).
- Emelie, P. Y., Phillips, J. D., Buller, B. & Venkateswaran, U. D. Free carrier absorption and lattice vibrational modes in bulk ZnO. *J. Electron. Mater.* **35**, 525–529 (2006).
- Miao, T. J. et al. In situ investigation of charge performance in anatase TiO₂ powder for methane conversion by Vis–NIR spectroscopy. *ACS Catal.* **11**, 8226–8238 (2021).
- Sarina, S. et al. Viable photocatalysts under solar-spectrum irradiation: nonplasmonic metal nanoparticles. *Angew. Chem. Int. Ed.* **53**, 2935–2940 (2014).
- Luo, L. et al. Binary Au–Cu reaction sites decorated ZnO for selective methane oxidation to C1 oxygenates with nearly 100% selectivity at room temperature. *J. Am. Chem. Soc.* **144**, 740–750 (2022).
- Liu, Q., Chen, T., Guo, Y., Zhang, Z. & Fang, X. Grafting Fe(III) species on carbon nanodots/Fe-doped g-C₃N₄ via interfacial charge transfer effect for highly improved photocatalytic performance. *Appl. Catal. B* **205**, 173–181 (2017).
- Xie, J. et al. Highly selective oxidation of benzene to phenol with air at room temperature promoted by water. *Nat. Commun.* **14**, 4431 (2023).
- Wang, K., Li, Y., Zhang, G., Li, J. & Wu, X. OD Bi nanodots/2D Bi₃NbO₇ nanosheets heterojunctions for efficient visible light photocatalytic degradation of antibiotics: enhanced molecular oxygen activation and mechanism insight. *Appl. Catal. B* **240**, 39–49 (2019).
- Li, B. et al. Water-participated mild oxidation of ethane to acetaldehyde. *Nat. Commun.* **15**, 2555 (2024).
- Song, S. et al. A selective Au-ZnO/TiO₂ hybrid photocatalyst for oxidative coupling of methane to ethane with dioxygen. *Nat. Catal.* **4**, 1032–1042 (2021).
- Chen, Z. & Wang, C. Rate constants of the gas-phase reactions of CH₃OOH with O₃ and NO_x at 293K. *Chem. Phys. Lett.* **424**, 233–238 (2006).
- Barnes, I., Becker, K. H. & Mihalopoulos, N. An FTIR product study of the photooxidation of dimethyl disulfide. *J. Atmos. Chem.* **18**, 267–289 (1994).
- Wallington, T. J. & Hurley, M. D. FTIR product study of the reaction of CD₃O₂+HO₂. *Chem. Phys. Lett.* **193**, 84–88 (1992).
- Zhang, W. et al. Light-driven flow synthesis of acetic acid from methane with chemical looping. *Nat. Commun.* **14**, 3047 (2023).
- Wang, J. et al. A highly selective and stable ZnO–ZrO₂ solid solution catalyst for CO₂ hydrogenation to methanol. *Sci. Adv.* **3**, e1701290 (2017).
- Fu, C. et al. Spontaneous bulk-surface charge separation of TiO₂-{001} nanocrystals leads to high activity in photocatalytic methane combustion. *ACS Catal.* **12**, 6457–6463 (2022).
- Chen, X. et al. Photocatalytic oxidation of methane over silver decorated zinc oxide nanocatalysts. *Nat. Commun.* **7**, 12273 (2016).
- Kresse, G. & Furthmüller, J. Efficient iterative schemes for ab initio total-energy calculations using a plane-wave basis set. *Phys. Rev. B* **54**, 11169–11186 (1996).
- Kresse, G. & Furthmüller, J. Efficiency of ab-initio total energy calculations for metals and semiconductors using a plane-wave basis set. *Comp. Mater. Sci.* **6**, 15–50 (1996).
- Perdew, J. P., Burke, K. & Ernzerhof, M. Generalized gradient approximation made simple. *Phys. Rev. Lett.* **77**, 3865–3868 (1996).
- Kresse, G. & Joubert, D. From ultrasoft pseudopotentials to the projector augmented-wave method. *Phys. Rev. B* **59**, 1758–1775 (1999).

Acknowledgements

J.T. acknowledges funding from the NSFC project (grant no. 22250710677) and the Beijing Municipal Project (grant no. C2022007). This project was also supported by the Tsinghua University Initiative Scientific Research Program. We also thank UK EPSRC (EP/S018204/2). Y.X. and C.W. acknowledge the UCL Dean's prize and the China CSC scholarship. T.Z., Q.Z. and L.G. thank the National Natural Science Foundation of China (grant nos. 22208021, 52250402 and 52322212).

Author contributions

J.T. created the concept and designed the overall project. J.T. and Y.L. supervised the progress of the whole project. Y.X. proposed the idea, designed and conducted the experiments, analysed the data and drafted the article. X.L. and C.W. assisted with the activity test and contributed to the discussion of the photocatalytic mechanism.

L.X. helped conduct the X-ray absorption fine structure spectra test. L.Z. helped conduct the in situ DRIFTS measurements. Q.Z. and L.G. carried out the STEM characterizations. T.Z. conducted the density functional theory calculations. All authors participated in the manuscript writing and approved the final version of the manuscript.

Competing interests

The authors declare no competing interests.

Additional information

Supplementary information The online version contains supplementary material available at <https://doi.org/10.1038/s41893-024-01401-y>.

Correspondence and requests for materials should be addressed to Tianyu Zhang, Yang Lan or Junwang Tang.

Peer review information *Nature Sustainability* thanks Wenlei Zhu and the other, anonymous, reviewer(s) for their contribution to the peer review of this work.

Reprints and permissions information is available at www.nature.com/reprints.

Publisher's note Springer Nature remains neutral with regard to jurisdictional claims in published maps and institutional affiliations.

Open Access This article is licensed under a Creative Commons Attribution 4.0 International License, which permits use, sharing, adaptation, distribution and reproduction in any medium or format, as long as you give appropriate credit to the original author(s) and the source, provide a link to the Creative Commons licence, and indicate if changes were made. The images or other third party material in this article are included in the article's Creative Commons licence, unless indicated otherwise in a credit line to the material. If material is not included in the article's Creative Commons licence and your intended use is not permitted by statutory regulation or exceeds the permitted use, you will need to obtain permission directly from the copyright holder. To view a copy of this licence, visit <http://creativecommons.org/licenses/by/4.0/>.

© The Author(s) 2024

Reporting Summary

Nature Portfolio wishes to improve the reproducibility of the work that we publish. This form provides structure for consistency and transparency in reporting. For further information on Nature Portfolio policies, see our [Editorial Policies](#) and the [Editorial Policy Checklist](#).

Statistics

For all statistical analyses, confirm that the following items are present in the figure legend, table legend, main text, or Methods section.

- | n/a | Confirmed |
|-------------------------------------|--|
| <input type="checkbox"/> | <input checked="" type="checkbox"/> The exact sample size (n) for each experimental group/condition, given as a discrete number and unit of measurement |
| <input type="checkbox"/> | <input checked="" type="checkbox"/> A statement on whether measurements were taken from distinct samples or whether the same sample was measured repeatedly |
| <input checked="" type="checkbox"/> | <input type="checkbox"/> The statistical test(s) used AND whether they are one- or two-sided
<i>Only common tests should be described solely by name; describe more complex techniques in the Methods section.</i> |
| <input checked="" type="checkbox"/> | <input type="checkbox"/> A description of all covariates tested |
| <input checked="" type="checkbox"/> | <input type="checkbox"/> A description of any assumptions or corrections, such as tests of normality and adjustment for multiple comparisons |
| <input type="checkbox"/> | <input checked="" type="checkbox"/> A full description of the statistical parameters including central tendency (e.g. means) or other basic estimates (e.g. regression coefficient) AND variation (e.g. standard deviation) or associated estimates of uncertainty (e.g. confidence intervals) |
| <input checked="" type="checkbox"/> | <input type="checkbox"/> For null hypothesis testing, the test statistic (e.g. F , t , r) with confidence intervals, effect sizes, degrees of freedom and P value noted
<i>Give P values as exact values whenever suitable.</i> |
| <input checked="" type="checkbox"/> | <input type="checkbox"/> For Bayesian analysis, information on the choice of priors and Markov chain Monte Carlo settings |
| <input checked="" type="checkbox"/> | <input type="checkbox"/> For hierarchical and complex designs, identification of the appropriate level for tests and full reporting of outcomes |
| <input checked="" type="checkbox"/> | <input type="checkbox"/> Estimates of effect sizes (e.g. Cohen's d , Pearson's r), indicating how they were calculated |

Our web collection on [statistics for biologists](#) contains articles on many of the points above.

Software and code

Policy information about [availability of computer code](#)

Data collection

Data analysis

For manuscripts utilizing custom algorithms or software that are central to the research but not yet described in published literature, software must be made available to editors and reviewers. We strongly encourage code deposition in a community repository (e.g. GitHub). See the Nature Portfolio [guidelines for submitting code & software](#) for further information.

Data

Policy information about [availability of data](#)

All manuscripts must include a [data availability statement](#). This statement should provide the following information, where applicable:

- Accession codes, unique identifiers, or web links for publicly available datasets
- A description of any restrictions on data availability
- For clinical datasets or third party data, please ensure that the statement adheres to our [policy](#)

The authors declare that all data supporting the findings of this study are available within the paper, supplementary information files and the provided source data files. Source data are provided with this paper.

Research involving human participants, their data, or biological material

Policy information about studies with [human participants or human data](#). See also policy information about [sex, gender \(identity/presentation\), and sexual orientation](#) and [race, ethnicity and racism](#).

Reporting on sex and gender	<input type="text" value="No applied to this study"/>
Reporting on race, ethnicity, or other socially relevant groupings	<input type="text" value="No applied to this study"/>
Population characteristics	<input type="text" value="No applied to this study"/>
Recruitment	<input type="text" value="No applied to this study"/>
Ethics oversight	<input type="text" value="No applied to this study"/>

Note that full information on the approval of the study protocol must also be provided in the manuscript.

Field-specific reporting

Please select the one below that is the best fit for your research. If you are not sure, read the appropriate sections before making your selection.

Life sciences Behavioural & social sciences Ecological, evolutionary & environmental sciences

For a reference copy of the document with all sections, see nature.com/documents/nr-reporting-summary-flat.pdf

Ecological, evolutionary & environmental sciences study design

All studies must disclose on these points even when the disclosure is negative.

Study description	<input type="text" value="This study is about selective methane conversion to HCHO using a cascade process comprising photocatalysis and thermodecomposition."/>
Research sample	<input type="text" value="This study uses single-atom Ru decorated ZnO as the catalyst."/>
Sampling strategy	<input type="text" value="Collect samples from both gas and liquid for analysis."/>
Data collection	<input type="text" value="Data is mainly recorded by using GC, NMR, XRD and UV-Vis spectra."/>
Timing and spatial scale	<input type="text" value="The major data was collected from Jan. 2023 to Mar. 2024."/>
Data exclusions	<input type="text" value="No data was exclude from the analyses."/>
Reproducibility	<input type="text" value="All attempts to repeat the experiment were successful"/>
Randomization	<input type="text" value="This is not relevant to this study because this study is about catalysis."/>
Blinding	<input type="text" value="This is not relevant to this study because this study is about catalysis."/>

Did the study involve field work? Yes No

Reporting for specific materials, systems and methods

We require information from authors about some types of materials, experimental systems and methods used in many studies. Here, indicate whether each material, system or method listed is relevant to your study. If you are not sure if a list item applies to your research, read the appropriate section before selecting a response.

Materials & experimental systems

n/a	Involvement in the study
<input checked="" type="checkbox"/>	<input type="checkbox"/> Antibodies
<input checked="" type="checkbox"/>	<input type="checkbox"/> Eukaryotic cell lines
<input checked="" type="checkbox"/>	<input type="checkbox"/> Palaeontology and archaeology
<input checked="" type="checkbox"/>	<input type="checkbox"/> Animals and other organisms
<input checked="" type="checkbox"/>	<input type="checkbox"/> Clinical data
<input checked="" type="checkbox"/>	<input type="checkbox"/> Dual use research of concern
<input checked="" type="checkbox"/>	<input type="checkbox"/> Plants

Methods

n/a	Involvement in the study
<input checked="" type="checkbox"/>	<input type="checkbox"/> ChIP-seq
<input checked="" type="checkbox"/>	<input type="checkbox"/> Flow cytometry
<input checked="" type="checkbox"/>	<input type="checkbox"/> MRI-based neuroimaging

Plants

Seed stocks

No applied to this study

Novel plant genotypes

No applied to this study

Authentication

No applied to this study